



HAL
open science

Complementarity of impact shot displacements and induced residual stress fields for a reliable estimation of crystal viscoplasticity parameters

S. Breumier, Fabrice Richard, Claire Maurice, Aurélien Villani, Guillaume Kermouche, Martin Lévesque

► To cite this version:

S. Breumier, Fabrice Richard, Claire Maurice, Aurélien Villani, Guillaume Kermouche, et al.. Complementarity of impact shot displacements and induced residual stress fields for a reliable estimation of crystal viscoplasticity parameters. 2020. hal-03019130

HAL Id: hal-03019130

<https://hal.science/hal-03019130>

Preprint submitted on 23 Nov 2020

HAL is a multi-disciplinary open access archive for the deposit and dissemination of scientific research documents, whether they are published or not. The documents may come from teaching and research institutions in France or abroad, or from public or private research centers.

L'archive ouverte pluridisciplinaire **HAL**, est destinée au dépôt et à la diffusion de documents scientifiques de niveau recherche, publiés ou non, émanant des établissements d'enseignement et de recherche français ou étrangers, des laboratoires publics ou privés.



Distributed under a Creative Commons Attribution 4.0 International License

Complementarity of impact shot displacements and induced residual stress fields for a reliable estimation of crystal viscoplasticity parameters

S. Breumier,^{1,3} F. Richard,² C. Maurice,¹ A. Villani,¹ G. Kermouche,¹ M. Lévesque³

¹Mines Saint-Etienne, Univ Lyon, CNRS, UMR 5307 LGF, Centre SMS, F - 42023 Saint-Etienne, France

²Univ. Bourgogne Franche-Comté, Institut FEMTO-ST, CNRS/UFC/ENSMM/UTBM, Département Mécanique Appliquée, F-25000 Besançon, France

³Département de Génie Mécanique, École Polytechnique de Montréal, C.P. 6079, Succ. Centre-ville, Montréal, Québec, H3C 3A7 Canada

Abstract

This work investigates the possibility to identify two crystal plasticity viscoplastic parameters K and n using two different outputs produced by the high velocity impact of a sphere onto a metallic sample: the shot displacement and the different components of the induced residual stress field on a cross-section under the dent. The identifiability of the two parameters using either the shot displacement, the residual stress field or the combination of both outputs is investigated using the sensitivity of each field to a variation of the coefficients as well as an identifiability indicator, I , representative of the problem well posedness.

This work demonstrates that identification of K and n using only the displacement curve is an ill-posed problem, even when combining the displacements obtained with different impact conditions. The residual stress field under the dent is proved to be rich enough to obtain the two coefficients using any of the in-plane stress components. Combining two stress components for identification results only in a slightly better conditioning of the problem. Finally, combining the shot displacement curve with a single component of the residual stress field obtained for the same test greatly improves the value of I . This result demonstrates that those two outputs provide complementary information for identification of the two coefficients.

Keywords: Identifiability analysis, Impact test, Crystal Plasticity Finite Element, Residual stress

This is an open access article under the CC BY license (<https://creativecommons.org/licenses/by/3.0/>)

Introduction

Crystal plasticity Finite Element (CPFE) frameworks such as the well-known Meric-Cailletaud model [20] provide insights on the strain mechanisms occurring at the grain scale considering the contribution of an average dislocation density on each slip system. Such models have been increasingly used for process modeling, such as shot-peening [9, 12, 21, 25], to predict the residual stress and hardening distributions induced at the grain scale, as it drives the material's fatigue behaviour [21, 27].

However, identification of the numerous material parameters involved in such frameworks represents a challenge due to the low scale involved in such simulation. Thorough identifiability analyses have therefore been performed by several authors [16, 22] to ensure that the tests used for identification contains sufficient information to represent the contribution of each parameters to the materials plastic behaviour.

In the seminal work of Meric et al. [20], identification was performed using cyclic tensile testing. However, the author did not investigate the well-posedness of the problem. Gerard et al. [15] performed identification of the Meric-Cailletaud interaction matrix coefficients using strain fields obtained by Digital Image Correlation (DIC) on tensile tests. Further analyses performed by Guery et al. [16] revealed that such methodology could only provide two isotropic hardening coefficients and three interaction matrix parameters. Renner et al. [22] investigated the identifiability of all the Meric-Cailletaud plastic parameters when using the residual topography left by Berkovich nanoindentations measured by Atomic Force Microscopy (AFM). Their study revealed that a single topography was not sufficient to obtain all the parameters. However, the authors demonstrated that combining three different topographies induced by indenting along three different crystal orientations would be sufficient to obtain the six interaction matrix parameters.

Identification of such parameters at high strain rates represent an additional challenge as it requires to perform high strain rate experiments at a small scale. It could however be of crucial importance when modeling manufacturing processes such as shot-peening as the process could involve strain rates up to 10^5 s^{-1} [19]. Previous studies modeling the process with crystal plasticity frameworks used parameters obtained with Split Hopkinson Pressure Bar (SHPB) tests [12, 25]. However SHPB is not local as the solicited volume ranges from a few cubic millimeters to a few cubic centimeters [2].

Breumier et al. [7] performed high strain rate microcompression tests to identify the Meric-Cailletaud viscoplastic parameters at the crystal scale. The authors obtained a unique solution of the parameters at high strain rates. However, the strain rate involved in the test was not higher than 10^2 s^{-1} which is a few order of magnitudes lower than the process range. Also, the Norton law used in the Meric-Cailletaud framework to represent the materials strain rate dependency represents an approximation that is only relevant on small strain rate ranges [18]. Identification in the process conditions is therefore necessary.

Single shot impacts have been scarcely used for material parameters identification [13].

The test however provides several outputs induced by high strain rate plastic deformations such as the shot displacement before and after the impact, the impact dent topography as well as the residual stresses induced by the impact. Indeed, advances over the past twenty years in High Resolution Electron BackScattered Diffraction (HR-EBSD) residual stress estimations opened the possibility to estimate stress variations under the impact dent that could be compared with Finite Element Analyses (FEA) [1, 9, 10].

This work investigates the possibility to identify the Meric-Cailletaud viscoplastic parameters using several outputs induced by controlled impact tests on copper single crystal specimen. This work is purely numerical and lays down the basis of an identification procedure using the outputs provided by a new shot peening test rig developed recently by the authors [8]. The test consists in projecting an industrial shot media onto a target surface with a wide range of velocities. The shot is filmed by two high frequency cameras and its three dimensional trajectory is reconstructed using an in-house code [5] with a 200 μm accuracy. The test therefore provides sufficient information to be reproduced in FEA. The shot displacement curve and the residual stress field measured by HR-EBSD under the impact dent could therefore be used for parameter identification.

This article is organized as follows: Section 1 details the numerical model and identifiability analysis methodology used in this study. Section 2 analyses the identifiability of the viscoplastic parameters using the shot displacement curve and the residual stress field under the impact dent. Section 3 discusses the results of the identifiability analyses and finally, section 4 concludes the work.

1 Methods

1.1 Material constitutive framework

The material constitutive behaviour which parameters are investigated is the Meric-Cailletaud large-strain formulation crystal plasticity framework [20]. The model was fully detailed in previous works [7, 9] but is here recalled for better readability. The deformation gradient \mathbf{F} is decomposed between its elastic and plastic contributions, respectively \mathbf{F}^e and \mathbf{F}^p , as:

$$\mathbf{F} = \mathbf{F}^e \cdot \mathbf{F}^p, \quad (1)$$

where \cdot denotes the dot product. The plastic part is related to the slips occurring in the different slip systems through

$$\dot{\mathbf{F}}^p \cdot (\mathbf{F}^p)^{-1} = \sum_{s=1}^N \dot{\gamma}^s \mathbf{m}^s \otimes \mathbf{n}^s, \quad (2)$$

where $\dot{\gamma}^s$ is the s -th slip system shear strain rate, N is the number of activable slip systems and \mathbf{m}^s and \mathbf{n}^s are unit vectors representing respectively the slip direction and the slip plane

h_1	h_2	h_3	h_4	h_5	h_6
Self-hardening	Coplanar	Hirth lock	Collinear	Glissile	Lomer junction
1	4.4	4.75	4.75	4.75	5

Table 1: Hardening interaction matrix parameters used for copper [20]

C_{11} (MPa)	C_{22} (MPa)	C_{44} (MPa)
159,300	122,000	81,000

Table 2: Elastic coefficients used for copper [20]

K (MPa s ^{1/n})	n	R_0 (MPa)	Q (MPa)	b
10.35	7.41	10	6	15

Table 3: Norton law and isotropic hardening parameters used for copper [7, 11]

normal.

The shear stress τ^s contributing to dislocation glide on a given system is related to the system's shear strain rate according to a Norton law where

$$\dot{\gamma}^s = \left\langle \frac{f^s(\tau^s)}{K} \right\rangle^n, \quad (3)$$

with $\langle . \rangle$ being the Macaulay brackets and K and n being material constants, that accounts for the material's strain rate sensitivity. An isotropic hardening term r^s is added to the flow rule f^s as

$$f^s = |\tau^s| - r^s. \quad (4)$$

The hardening term r^s results from the interactions between the different dislocation slip systems modeled by

$$r^s = R_0 + \sum_{q=1}^N h_{sq}(R_q - R_0), \quad (5)$$

with

$$R_q = R_0 + Q(1 - e^{-v^q b}), \quad (6)$$

where R_0 is the critical resolved shear stress, Q and b are two phenomenological constants, v^q is the accumulated plastic slip for the q -th system and h_{sq} is the interaction coefficient between systems (s) and (q).

Most of the constitutive parameters used as a reference in this study are those provided in the work of Casals et al. [11]. The values of the K and n coefficients are those identified by Breumier et al. [7] using high strain rate microcompression experiments. Tables 1, 2 and 3 summarizes the different coefficients used in this study.

1.2 Finite element model

The impact is modeled using Abaqus dynamic explicit solver with an automatic time step procedure. The model geometry and mesh is presented in Figure 1. The mesh is divided in three different zones: (i) a refined mesh zone close to the contact to accurately describe the stress gradient in the plastic zone, (ii) an extended mesh zone surrounding the refined mesh zone to limit border effects and (iii) an infinite CIN3D8 element mesh zone surrounding the geometry to damp residual elastic stress waves. The mesh is blocked at the bottom and an initial velocity V_0 is imposed to the shot. The total simulation time is taken as two times the impact duration to ensure that the obtained residual stress field is at equilibrium.

The size of the refined mesh zone is chosen so as to contain all the plastic deformations following the same methodology as the one presented by Breumier et al. [9]. The substrate is modeled using linear reduced integration hexahedric elements (C3D8R) to prevent locking effects due to incompressible plastic flow [14]. The mesh density is chosen by a convergence study based on the displacement curve and the residual stress field sensitivity as further detailed in Appendix A and in section 2.2.

The shot to be used in future experiments will be 1 mm 440C stainless steel bearing balls. The shot is therefore modeled as infinitely rigid as copper is very ductile and less rigid than the shot material. The contact between the shot and the sample is modeled using Abaqus general contact with a hard contact normal component and a penalty frictional tangential component with a friction coefficient of 0.2. Only half of the shot is modeled and its moment of inertia I_M is calculated as:

$$I_M = \frac{2}{5}m_{shot}r^2, \quad (7)$$

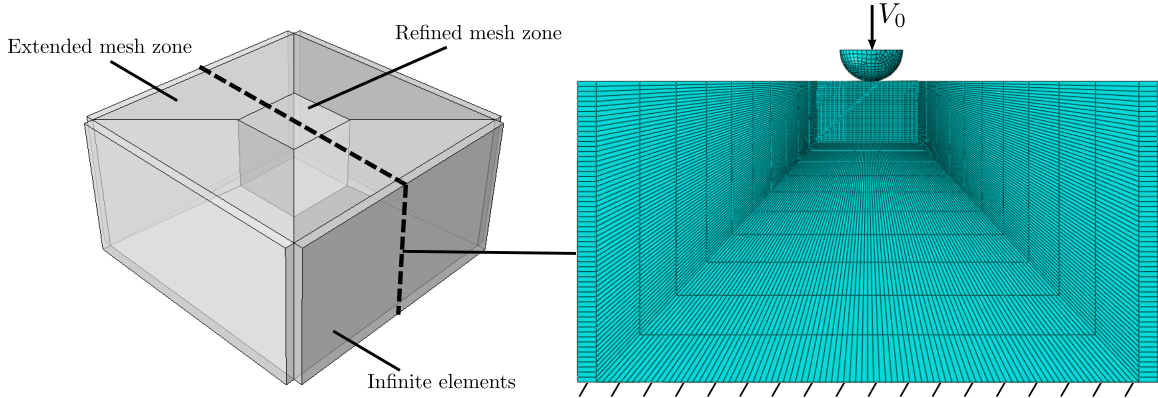


Figure 1: Finite element model used for impact simulations. The sample geometry is divided in three zones: a refined mesh zone at the impact location, surrounded by an extended mesh zone to limit the effect of boundary conditions and infinite elements around the sample to damp residual stress field oscillations. An initial velocity V_0 is imposed to the shot.

Test name	Crystal orientation	Shot velocity (m s ⁻¹)
Condition 1	[100]	40
Condition 2	[100]	80
Condition 3	[110]	40

Table 4: Modeled impact test conditions

where m is the shot mass estimated as:

$$m_{shot} = \rho_{shot} \frac{4}{3} \pi r^3, \quad (8)$$

where r is the shot radius and ρ_{shot} is the shot density taken as 7.110^{-3} g mm⁻³. The initial shot velocity is imposed at the rigid body reference point with values of successively 40 m s⁻¹ and 80 m s⁻¹ to study the influence of the strain rate on the identifiability.

The sample material is modeled using the Meric-Cailletaud crystal plasticity finite element framework [20] detailed in section 1.1. Impacts are simulated with the impacted surface normals oriented successively along the [100] and [110] crystal orientations to study the influence of crystal plasticity anisotropy on parameters' identifiability. Table 4 summarizes the three different impact conditions tested. Copper density is taken as $8.98 \cdot 10^{-3}$ g mm⁻³.

1.3 Identifiability analysis

Assessing the possibility to identify a model constitutive parameters using a given set of observations consists in demonstrating that the problem to solve is well-posed *e.g.* (i) that there is a reasonably low number of admissible solutions, (ii) that each identified parameters have a distinct influence on the model's outputs and (iii) that those outputs are sufficiently sensitive to each of the parameters with similar amplitudes. These conditions are investigated for the identification of the Meric-Cailletaud K and n viscoplastic parameters using either the shot displacement $u(t)$ or the residual stress field in the cross section under the impact dent.

A typical numerical unidirectional shot displacement curve is shown in Figure 2. The curve can be divided in three parts:

- Before impact where the shot velocity v_{before} is almost constant.
- During the impact where the velocity decreases and changes sign when the shot starts to rebound.
- After impact where the shot velocity v_{after} reaches a lower constant value.

The velocity measured before and after the impact, combined with the impact event duration, are representative of the energy absorbed by the material during the impact which is mainly dissipated by plastic deformation and elastic wave propagation, if temperature effects are negligible [17].

In reality, the shot trajectory is three dimensional and three different curves have to be analyzed for the three different space directions. However, this study only focuses on unidirectional impacts as it only aims at laying the basis of an identifiability analysis and identification methodology.

The displacement curve sensitivity to a constitutive parameter variation is defined as follows:

$$\frac{\partial \bar{u}}{\partial \theta_i}(t) = \frac{1}{\max(|u|)\epsilon\sqrt{T}} (u(\theta_i + \epsilon\theta_i, t) - u(\theta_i, t)), \quad (9)$$

where $u(t)$ is the shot displacement at time t , ϵ is the perturbation factor, θ_i is the constitutive parameter to be identified and T is the number of acquisition points taken as 100. The overline notation designates dimensionless quantities, as u and θ_i are rendered dimensionless in equation 9 respectively by dividing by $\max(|u|)$ and by the use of a dimensionless perturbation factor ϵ .

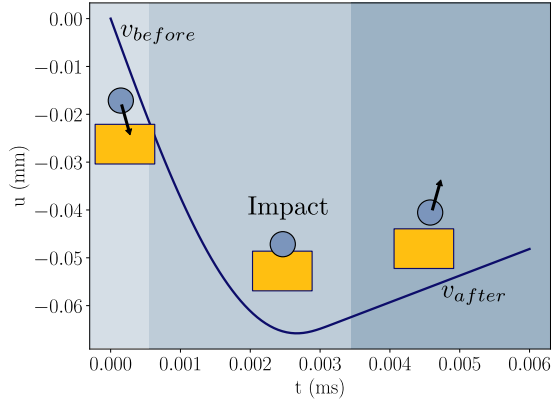


Figure 2: Typical single impact displacement curve with respect to time obtained by finite element simulations. The shot velocity v_{before} is constant before the impact. Then, it progressively decreases and changes sign when the shot starts to rebound to finally reach a constant velocity v_{after} after the impact.

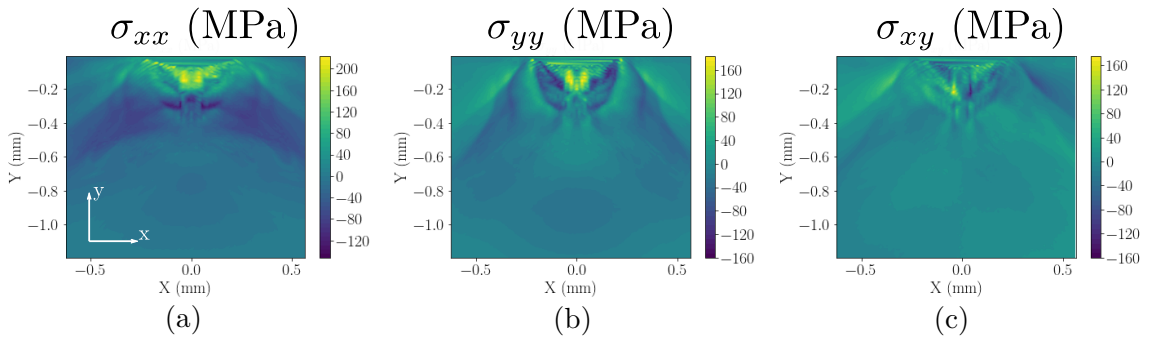


Figure 3: Typical residual stress field in the cross-section under the impact dent obtained for the reference material after an impact of a shot propelled at $40 \text{ m}\cdot\text{s}^{-1}$ along the $[100]$ crystal orientation and interpolated on a 80×80 regular grid. (a) σ_{xx} , (b) σ_{yy} and (c) σ_{xy} components.

Figures 3 (a), (b) and (c) show respectively the variation of the σ_{xx} , σ_{yy} and σ_{xy} residual stresses under the impact dent obtained numerically using the reference material's coefficient, for an impact along the [100] crystal orientation at $40 \text{ m}\cdot\text{s}^{-1}$. The identifiability analysis is conducted on the stress values at the integration point of elements positioned in the cross-section of the middle of the impacted sample. As future identification will be performed by comparing numerical results with experimental EBSD fields, the stress field at the integration point is linearly interpolated on a regular square grid. A 80×80 grid is used for the identifiability analysis to match with the grid size used for the finite element simulation. Note that linear interpolation is chosen to remain consistent with the use of C3D8R elements.

The sensitivity of a given stress component σ_{ij} under the impact dent center, to a variation of parameter θ , is defined as:

$$\frac{\partial \overline{\sigma}_{ij}}{\partial \theta}(x, y) = \frac{1}{\max(|\sigma_{ij}|)\epsilon\sqrt{N}} (\sigma_{ij}(\theta + \epsilon\theta, x, y) - \sigma_{ij}(\theta, x, y)), \quad (10)$$

where N is the number of sampled points on the grid taken as 6400, x and y are the 2D spatial coordinates in the cross-section plane. Note that a constant uncertainty is assumed both for the stress and shot displacement value in equations 9 and 10 as the sensitivity value is normalized by the maximum value of u and σ_{ij} to provide sensitivity values that can be compared for output of different natures. The absolute variation of each output is considered instead of the relative one, as the latter would have given too much weight to low displacement and stress values. Indeed, low displacement values represents the contact onset and the end of the contact where no plastic straining occurs. Low residual stress values are also found in the sample where no deformation event occurs.

The sole analysis of the sensitivity values is not sufficient to assess that a problem solution is unique and stable. The identifiability of the identified coefficients is therefore assessed in this work by computing the identifiability index I presented in the work of Richard et al. [23], defined as:

$$I = \log_{10} \left(\frac{\lambda_{max}}{\lambda_{min}} \right), \quad (11)$$

where λ_{max} and λ_{min} are the extremal eigenvalues of the approximated dimensionless hessian matrix close to the cost function minimum, defined as:

$$\overline{H}_{ij} = \sum_{p=0}^N \frac{\partial \overline{y}}{\partial \theta_i}(x_p) \frac{\partial \overline{y}}{\partial \theta_j}(x_p), \quad (12)$$

where N is the number of acquisition points, $\frac{\partial \overline{y}}{\partial \theta_i}(x_p)$ is the sensitivity of the observation y to the parameter θ_i for the acquisition point x_p . In the above, $y(x_p)$ can therefore designate either $u(t_p)$ or $\sigma_{ij}(x_p, y_p)$. According to Richard et al. [23], a value of $I < 2$ is representative of a good conditioning of the inverse problem. Note that this value is only an indication. In practice, I provides a quantitative comparison of the wealth of information given by various

observation fields, considering that, the lower the value, the better the problem will be posed.

2 Results

2.1 Displacement curves

Figure 4 (a) shows the evolution of the displacement sensitivity with respect to time when varying the coefficients K and n respectively by 5% of their initial values. The figure reveals that K and n have an opposite influence on the displacement. However, the absolute value of the sensitivity is very similar for the two variables, suggesting a strong correlation of their

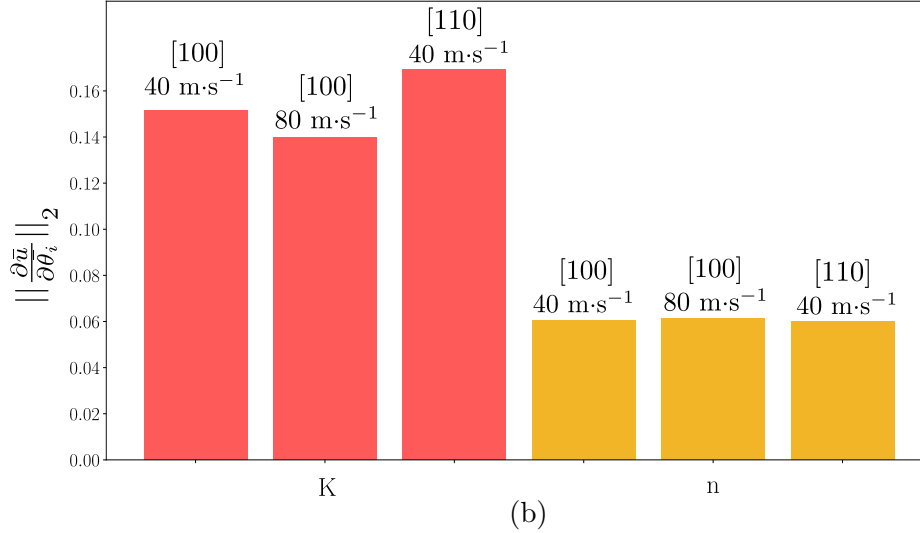
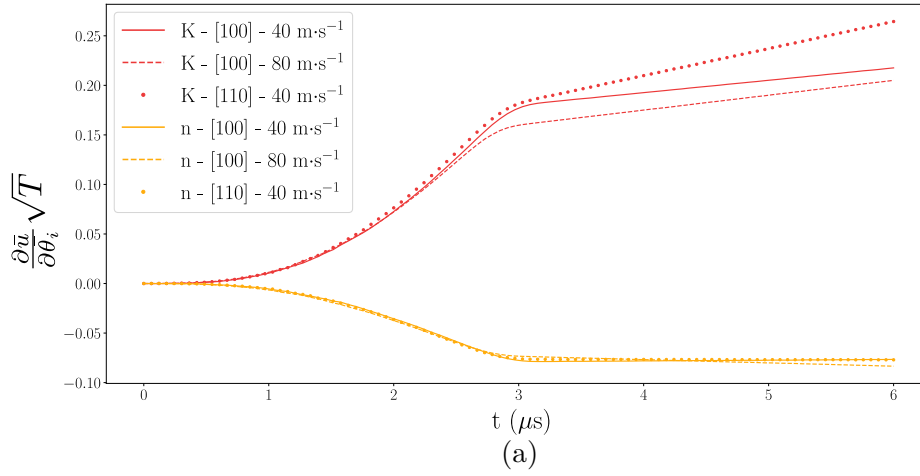


Figure 4: Sensitivity of the displacement to a 5% variation of K and n for a shot propelled at 40 m s^{-1} along the $[100]$ orientation, at 80 m s^{-1} along the $[100]$ orientation and at 40 m s^{-1} along the $[110]$ orientation. (a) Evolution with respect to time of the sensitivity of the displacement to a 5% variation of K and n . (b) L_2 norm of the sensitivity variation over the whole time domain. The displacement curve is at least twice as sensitive to a variation of K than a variation of n . The two variables present a similar absolute sensitivity variation.

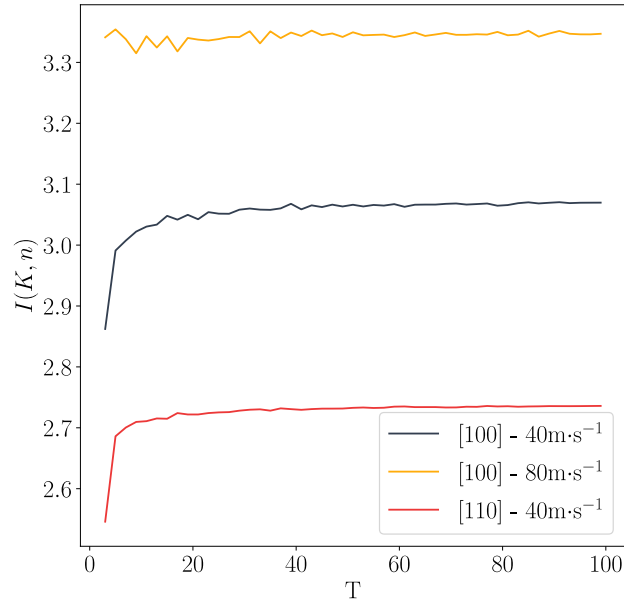


Figure 5: Evolution of I with the number of acquisition points. The value of I converges to a constant value for a very low number of acquisition points for the three test conditions.

influence on the shot displacement. Figure 4 (b) shows the L_2 norm of the sensitivity for the two variables. The figure reveals that K has a much stronger influence on the displacement than n for the tested impact conditions.

The value of I was computed for different values of T , to ensure its independence on the number of acquisition points. Figure 5 shows the variation of I for the three test conditions as a function of the number of acquisition points. The values of I is stable and converges for a very low number of acquisition points. This results from the fact that only the slope of the displacement curve after the impact is influenced by a variation of K and n , which can be described with a low number of acquisition points.

The value of I obtained for a perturbation of 5% with an initial shot velocity of 40 m s^{-1} along the [100] orientation (condition 1) was $I = 3.1$. This confirms that identification using only the shot displacement curve is an ill-posed problem as the two variables have opposite but very similar effects on the displacement. The number of possible solution for K and n is therefore large when using only a single shot displacement curve.

Velocity (m s^{-1})	Orientation	I
40	[100]	3.1
80	[100]	3.3
40	[110]	2.7

Table 5: Values of I obtained for the three different conditions.

However, the problem well-posedness could be improved by changing the test conditions such as the impact velocity or the crystal orientation. To illustrate this point, similar simulations have been performed along the [100] orientation with a velocity of 80 m s⁻¹ (condition 2) and along the [110] orientation with a velocity of 40 m s⁻¹ (condition 3).

Figures 4 (a) and (b) show the sensitivity evolution with time and the sensitivity norms for the three conditions. The figure reveals that changing both the crystal orientation and velocity has a higher influence on the absolute variation of K than to a variation of n .

Table 5 shows the values of I obtained for the three different conditions. For a given crystal orientation (*e.g.* [100]), a higher velocity value leads to a higher value of I . This result shows that as the velocity increases, the correlation between the sensitivities of the shot displacement to K and n also increases, which has a negative impact on the identifiability. Inversely, changing the orientation reduces the value of I which shows that it tends to decorelate the effect of the two variables.

To investigate the influence of the combination of two different tests on the identifiability value, the hessian matrix was computed as:

$$\overline{H}_{ij}^{kl} = \sum_{p=0}^T \frac{\partial \overline{u}_k}{\partial \theta_i}(t_p) \frac{\partial \overline{u}_k}{\partial \theta_j}(t_p) + \sum_{p=0}^T \frac{\partial \overline{u}_l}{\partial \theta_i}(t_p) \frac{\partial \overline{u}_l}{\partial \theta_j}(t_p), \quad (13)$$

where u_k and u_l corresponds to the displacement obtained for two of the conditions detailed

	80 m s ⁻¹ /[100]	40 m s ⁻¹ /[110]
40 m s ⁻¹ /[100]	3.0	2.7
80 m s ⁻¹ /[100]		2.6

Table 6: Values of I obtained for the combination of two different conditions.

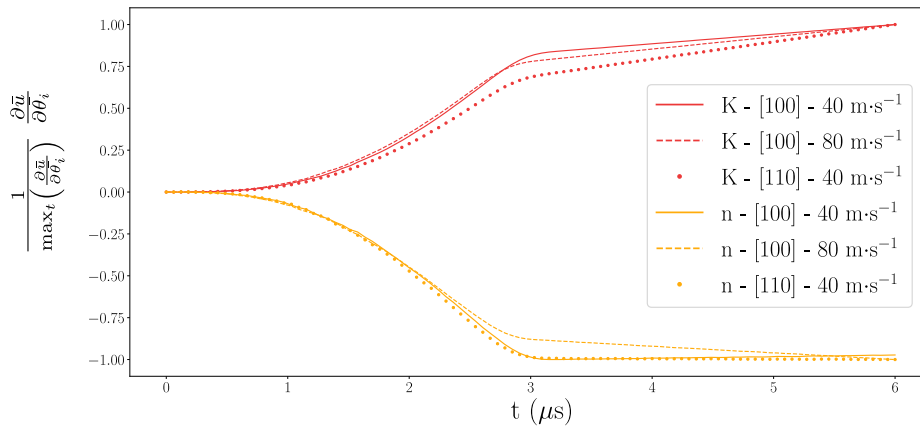


Figure 6: Relative sensitivity of the displacement to a 5% variation of K and n for the three different test conditions. Changing the shot velocity has a larger relative influence on the sensitivity of the displacement to a variation of n than to a variation of K and inversely when changing the crystal orientation.

in table 4. The values of I obtained when combining the three different tests two by two are presented in Table 6. Note that adding information did not result in an improvement of the identifiability in every case. The best value of I is 2.6 and is obtained when combining two different crystal orientations with two different shot velocities.

To better understand this result, Figure 6 shows the variation of the sensitivity of the displacement to a 5% variation of K and n relatively to the maximum sensitivity value for each conditions and variables. The figure reveals that changing the impact velocity has a higher influence on the relative displacement sensitivity to a variation of n than to a variation of K . Inversely, changing the crystal orientation has a higher influence on the sensitivity to a variation of K than to a variation of n .

However, the highest value of I obtained is not sufficiently low to lead to a well posed problem.

2.2 Residual stress field

2.2.1 Extracting relevant sensitivity information

The sensitivity of the σ_{xx} component of the stress for an impact along the [100] orientation at $40 \text{ m}\cdot\text{s}^{-1}$ is first considered, to investigate the different treatments that should be performed on the residual stress field before using it for identifiability analyses. Indeed, as opposed to the previous section, the identifiability analysis is performed on a two dimensional field which makes the influence of numerical noise on the sensitivities correlation more difficult to evidence. The two dimensional sensitivity variations for the two variables cannot be superposed as in Figure 4 on a one dimensional plot to visually observe a potential correlation of the sensitivities.

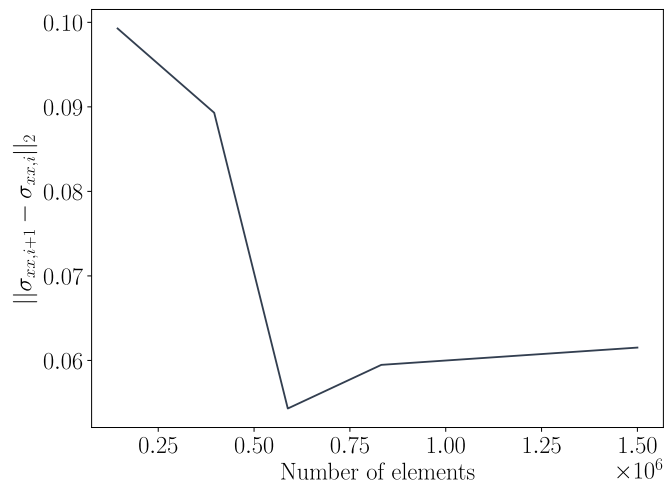


Figure 7: Evolution of the L_2 norm of the difference between the σ_{xx} fields obtained with two successive meshes. Convergence is observed for 832 000 elements.

Also, dynamic explicit analyses induce numerical uncertainties as no residual is minimized over the analysis [3]. Such uncertainties accumulate with the time steps resulting in small erratic variations of the final field which should not be physically interpreted. This effect should be even stronger when non-linear behaviors are involved such as contact or plasticity. The influence of numerical uncertainties on the sensitivity should therefore be investigated to account only for the parts of the sensitivity field that have a physical sense. This is not only important to assess the well-posedness of the problem but also for the identification itself to prevent the identification to be driven by numerical uncertainties that have no physical meaning.

Figure 7 shows the evolution of the L_2 norm of the difference in horizontal components of stress σ_{xx} between two consecutive meshes for an impact along the [100] orientation at $40 \text{ m}\cdot\text{s}^{-1}$. The figure reveals that the stress field converges for 832 000 elements, which is consistent with the convergence study performed on the shot displacement detailed in Appendix A. However the sole convergence of the stress field is not sufficient to obtain converged sensitivity values. Figure 8 shows the σ_{xx} sensitivity to a variation of 5% of the K coefficient for different mesh densities. The figure reveals that the sensitivity field does not seem to converge qualitatively in a half sphere under the dent with a radius close to that of the contact.

Sensitivity values in this zone are highly sensitive to numerical uncertainties and convergence errors which result in noisy sensitivity variations. Using the field without masking

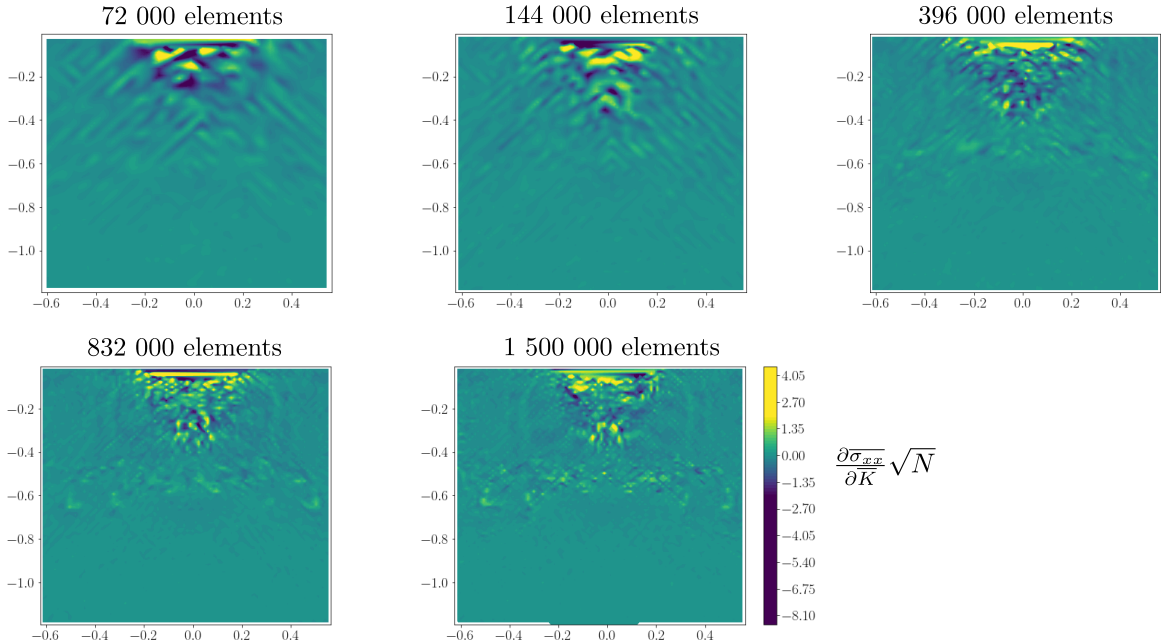


Figure 8: Evolution of the sensitivity of σ_{xx} to a variation K with the number of elements. The sensitivity underneath the impact dent does not converge to a consistent shape.

the noisy sensitivity values under the dent would thus artificially decorrelate the influence of the identified coefficients on the residual stress field [6]. Such errors could result from the explicit integration scheme, contact integration errors but also from the strong plastic strain gradients present in such zone that could not be captured with the current mesh. This zone should therefore not be used for identification of K and n as the stress variations would not entirely result from a variation of each coefficients. In the following, a spherical mask, with a radius close to that of the contact, is therefore applied to the sensitivity field to exclude the zone where the sensitivity field does not converge.

To understand the influence of the different parts of the residual stress field on the identifiability, the value of I should be computed on a well chosen path that conveniently separates the different zone of interests of the field. The path chosen is represented in Figure 9. Only the refined zone of the mesh is studied as no stress is present in the extended mesh zone. The path is going back and forth between the left and the right side of the residual stress field and moves progressively toward the impact dent where most of the plastic deformations occurred.

The sensitivity of σ_{xx} to a variation of 5% of K and n are presented in Figure 10 (a) and (b). The evolution of I as the length of the path represented in Figure 9 increases (from top to bottom) is presented in Figure 10 (c). The value of I is very low when compared to that obtained with micropillar compression curves in previous work [7], even at the bottom of the sample where almost no plastic straining occurred.

The variations of the sensitivity at the bottom of the sample, along the path shown in Figure 9, up to the point A indicated in Figure 10, are shown in Figure 11. The average sensitivity to K and n are slightly different at the bottom of the sample, which could partially explain the low value of I found in this zone. However, the amplitude of the noise on the sensitivity variations are of the same order of magnitude as that of the average difference

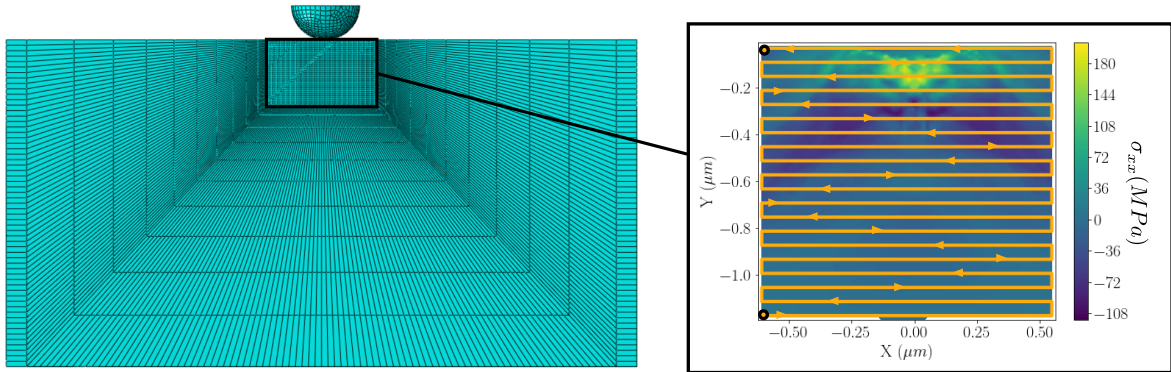


Figure 9: Path chosen to compute the values of I on different parts of the field. Only the refined zone of the mesh was studied as no stresses were present on the extended mesh zone. The path is going back and forth between the left and the right side of the residual stress field and moves progressively toward the impact dent.

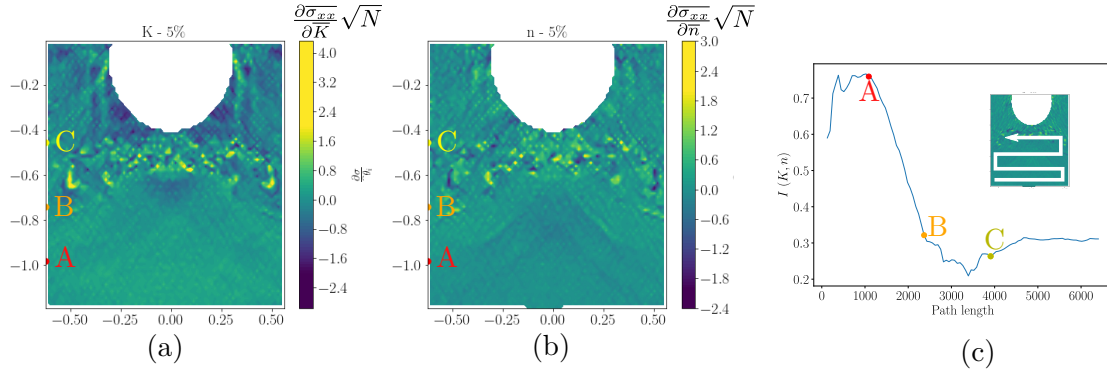


Figure 10: Sensitivity of σ_{xx} to a 5% variation of (a) K and (b) n . The two variables have a distinct influence on σ_{xx} as its sensitivity variations to K and n are not similar. (c) Evolution of the value of I computed on a path starting from the bulk and going progressively to the surface with the path length. The very low value of I results from the noisy variation of the sensitivities which artificially decorrelates the influence of the two variables.

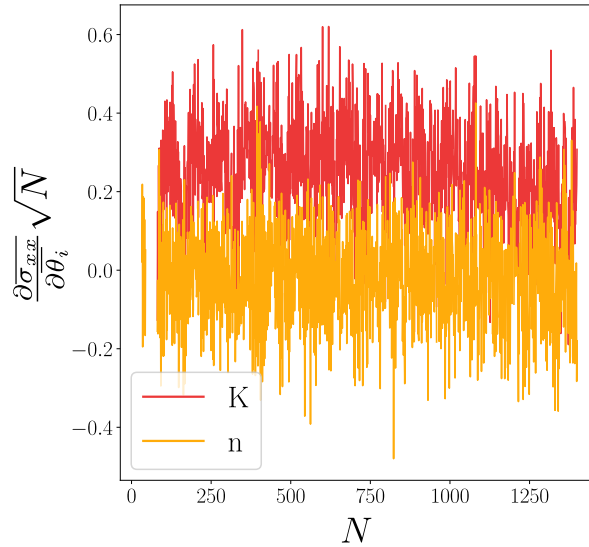


Figure 11: Sensitivity variation of σ_{xx} to a 5% variation of K and n on the path shown in Figure 9 at the bottom of the sample, up to the point A indicated in Figure 10. The noise on the sensitivity variation is of the same order of magnitude than the average value of the sensitivities, which artificially decorrelates the influence of the two coefficients.

between the sensitivity of K and n . This reveals that the residual stress field is still too noisy to compute relevant values of the identifiability indicator, as this noise is sufficiently substantial to artificially decorrelate the influence of the two variables.

Figures 12 and 13 show the variation of the σ_{xx} sensitivity field for different values of perturbation of K and n respectively. The figures show that the sensitivity field is relatively noisy for low values of the perturbation. This could result from the use of a dynamic explicit finite element scheme introducing numerical uncertainties of the same order as that of the sensitivity for low perturbation values.

The sensitivity fields for perturbations larger than 15% also reveal that K and n have a non colinear effect on σ_{xx} as the two variables induce different sensitivity variations. However such observation does not provide enough information to state on the problem well-posedness. It only implies that the influence of the two coefficients on σ_{xx} can be differentiated but not that the information is rich enough to obtain the two coefficients values simultaneously.

To illustrate the influence of noise, a Hamming window is applied on the residual stress field Fourier transform to filter the high frequency noise [4]:

$$\omega(x_i, y_i) = \left[\left(0.54 - 0.46 * \cos \left(\frac{2\pi x_i}{\sqrt{N} - 1} \right) \right) \left(0.54 - 0.46 * \cos \left(\frac{2\pi y_i}{\sqrt{N} - 1} \right) \right) \right]^r, \quad (14)$$

Where x_i and y_i are the discrete spatial coordinate on the field and r is a factor controlling the window radius (*e.g.* the filter bandwidth).

Figure 14 shows a comparison of the sensitivity of σ_{xx} to K for different perturbation values using a low pass filter with a hamming window radius of 10. Filtering removes the differences between the high and low perturbations at least down to perturbation values of 10%. Figures 15 (a) and (b) show the sensitivity of σ_{xx} to K and n to a perturbation of 15%. Figure 15 (c) shows the variation of I on a path going from the bulk to the surface. Using the filter results in more believable values of I at the bottom of the field.

Up to point A, the value of I progressively rises as the sensitivity fields are almost constant in this zone but with distinct values for the two coefficients. From point A to point B, a large decrease of I is observed down to a value of 0.7. This is consistent with the variations of the

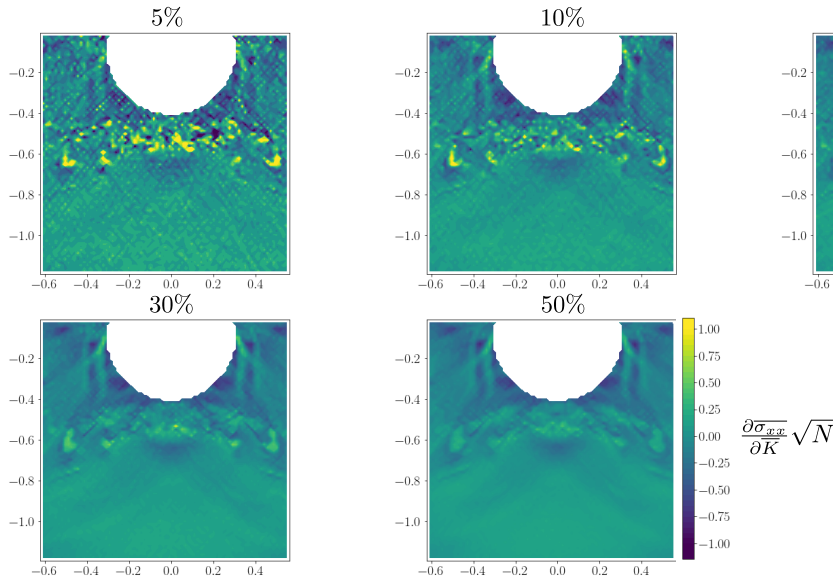


Figure 12: Sensitivity of σ_{xx} to a variation K for different perturbation factor (5%, 10%, 15%, 30%, 50%). The noisy variation of the sensitivity for low perturbation value result from low stress variations of the same order of magnitude than the numerical uncertainties.

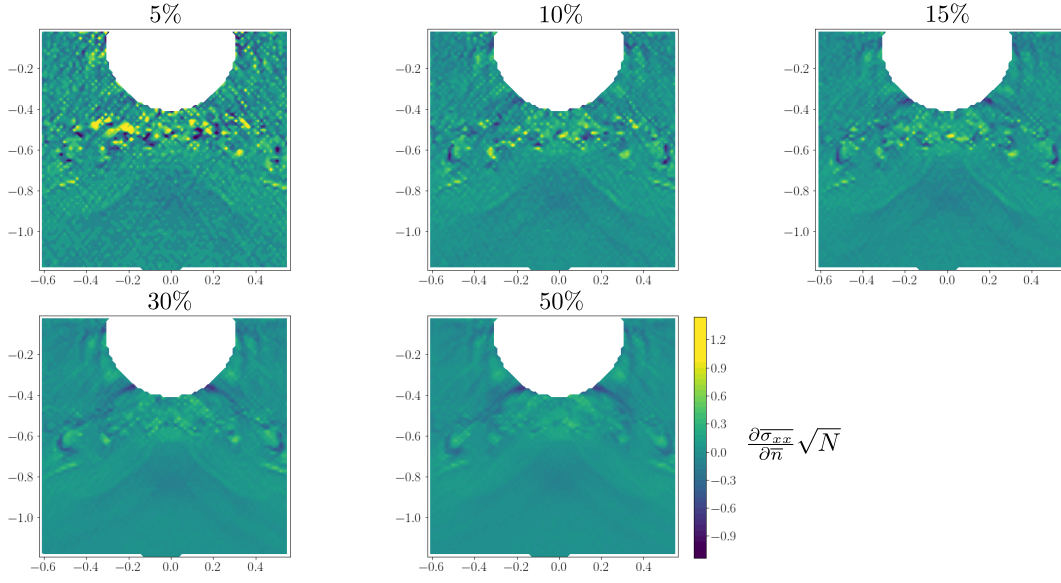


Figure 13: Sensitivity of σ_{xx} to a variation n for different perturbation factor (5%, 10%, 15%, 30%, 50%). The sensitivity field for the higher perturbation are different than those obtained for a perturbation of K . This confirms the low correlation of the two variable effects.

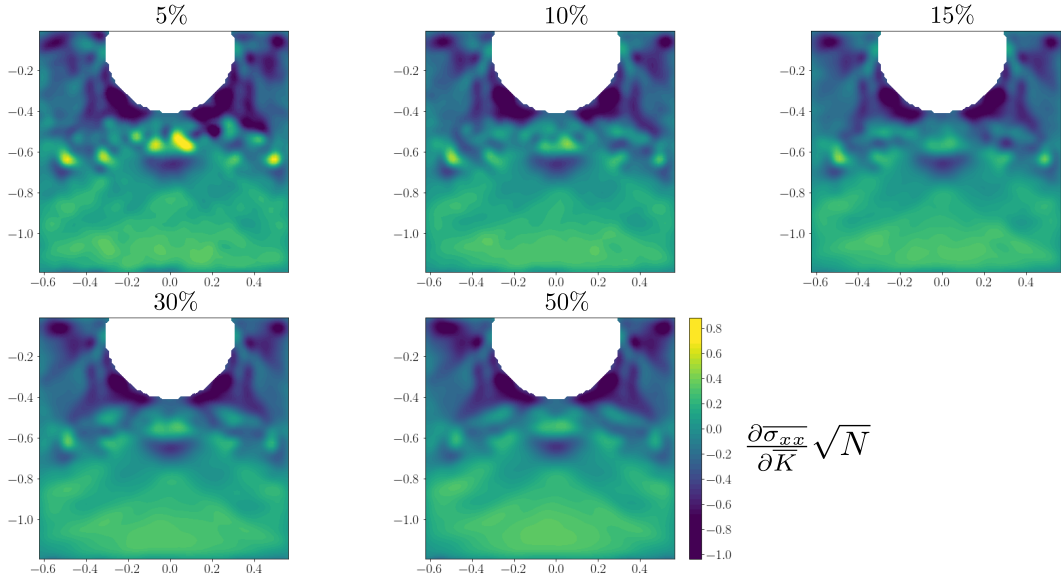


Figure 14: Sensitivity of σ_{xx} to a variation K for different perturbation factor (5%, 10%, 15%, 30%, 50%) after applying a low-pass filter with a radius of 10. The filter smoothed the variation of the sensitivities and removes the noise down to perturbation of 10%.

sensitivity field observed in Figures 15 (a) and (b) as both variables seem to have a different influence on this part of the field, with similar amplitudes. Between point B and C, a small decrease of I is also observed due to higher variations of both sensitivity fields in different directions.

To assess the value of I independently of the Hamming window radius, the value of I obtained using the whole σ_{xx} field is computed for different window radius. Figure 16 (a) shows the evolution of I with the filter radius. The figure reveals that the value of I follows an inverse exponential tendency and saturates for a radius of 1000.

To ensure that the value of I at saturation does not result from the Fourier space resolution being too low, the value of I is computed with a filter radius of 3000 for different grid sizes. To ensure that the value of I at saturation does not result from the Fourier space resolution being too low, the value of I is computed with a filter radius of 3000 for different grid sizes.

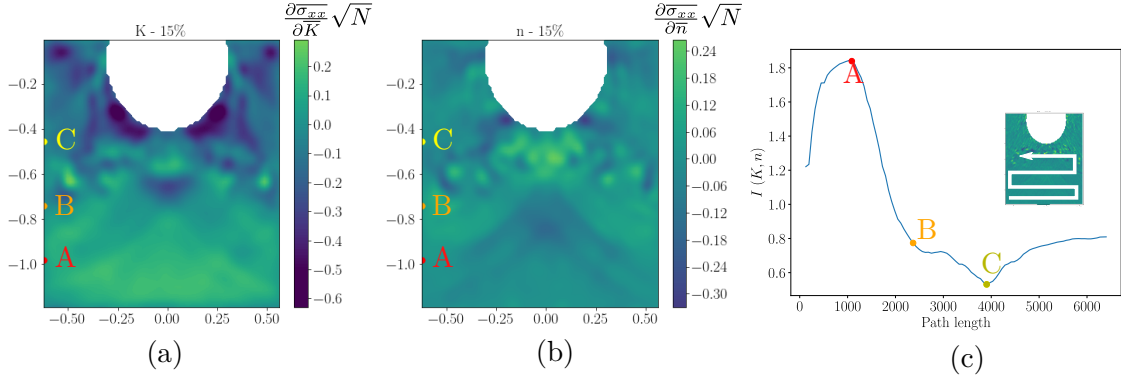


Figure 15: Sensitivity of σ_{xx} to a 15% variation of (a) K and (b) n after applying a low-pass filter with a radius of 10. (c) Evolution of the value of I computed on a path starting from the bulk and going progressively to the surface with the path length. The low pass filter allows to find more realistic values of I .

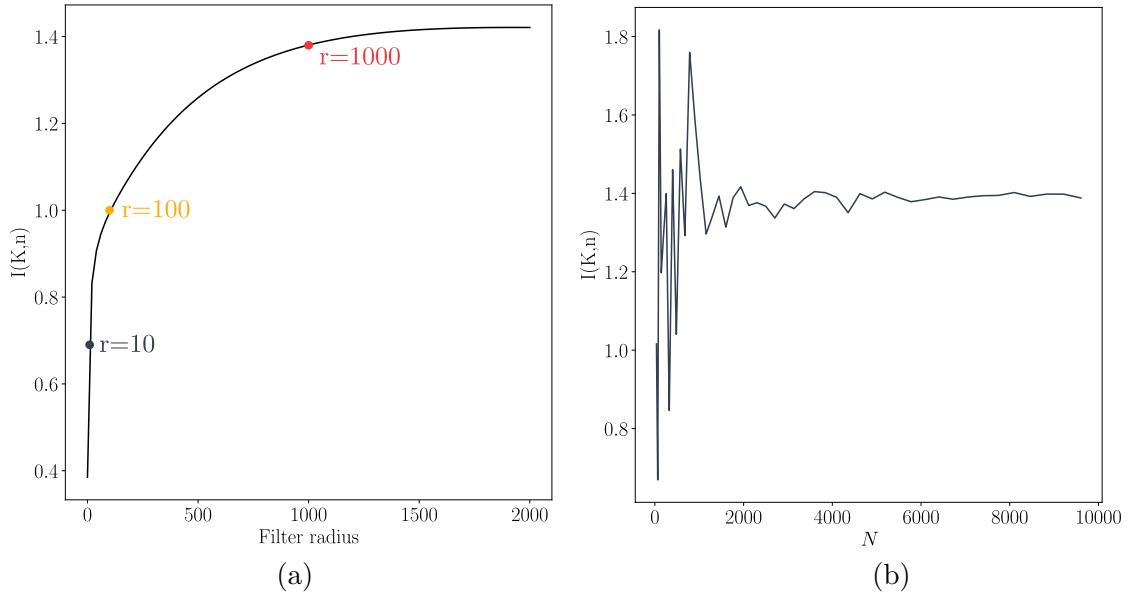


Figure 16: Influence of the filter on I . (a) Variation of I with the Hamming window radius. (b) Variation of I for large Hamming window radius with the grid size. For large window radius, the value of I saturates to a constant value. This constant value converges with the grid size for 50 points on one side of the grid.

Figure 16 (b) shows the evolution of the value of I with the number of points on one side of the square grid. The value of I at saturation oscillates with the mesh size until 4000 points, which is a lower resolution than the finite element grid size on which the stress is interpolated. Therefore the saturation of I does not result from the resolution of the Fourier space being too coarse.

Figure 17 shows the variation of the sensitivity to (a) K and (b) n for different window radius r on the path shown in Figure 10. The figure shows that the sensitivity variations obtained for a large value of r represents the average variation of the non filtered sensitivity. Therefore, the value of I is representative of the average sensitivity of σ_{xx} to K and n . The filter only removes the high frequency variations of the field and does not add spurious information. The corresponding value of I for the three filter radius are represented by color dots in Figure 16.

The value of I obtained for large filter radius can therefore be considered a higher boundary of the identifiability index value that can be obtained. In the following, the value of I given for the residual stress field will therefore be the value of I that saturates with the Hamming window radius.

To investigate the potential complementarity of the information provided by the shot displacement and the residual stress field, the value of I obtained when combining the two

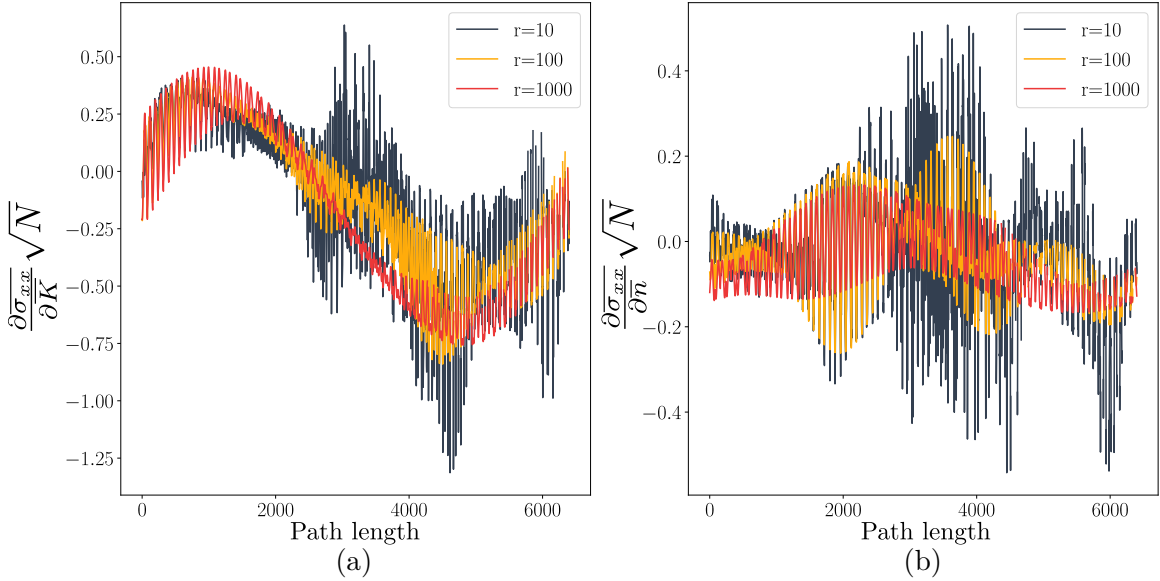


Figure 17: Sensitivity of σ_{xx} to 15% a variation of (a) K and (b) n with respect to the path length for different filter radius r . The sensitivity for high filter radius represents the average sensitivity variation of the non filtered field.

observation fields is computed using the following expression for the hessian matrix:

$$\bar{H}_{ij} = \sum_{p=0}^T \frac{\partial \bar{u}}{\partial \theta_i}(t_p) \frac{\partial \bar{u}}{\partial \theta_j}(t_p) + \sum_{p=0}^N \frac{\partial \bar{\sigma}_{xx}}{\partial \theta_i}(x_p, y_p) \frac{\partial \bar{\sigma}_{xx}}{\partial \theta_j}(x_p, y_p). \quad (15)$$

Note that, in the above expression, the same weight is given to both fields as all the variables are dimensionless. The combination of the two observation fields for the same impact along the [100] orientation at 40 m·s⁻¹ leads to $I = 1.1$ which is slightly better than the value obtained using only the residual stress field ($I = 1.4$).

2.2.2 Influence of the stress component

A similar methodology is applied to study the identifiability of K and n using the other components of the residual stress field induced by an impact. As experimental residual stress estimations is to be provided by EBSD analyses, only the in-plane components of the stress tensor is investigated. Figures 18 and Figures 19 (a), (b) and (c) show respectively the sensitivity of σ_{yy} and σ_{xy} to a 15% variation of K and n and the resulting variation of I along a path. Similar conclusions as with σ_{xx} can be drawn. Also, low values of I are found at the bottom of the field resulting from large differences in the influence of the two variables on this stress component.

Table 7 summarizes the value of I obtained using every grid points for large values of the filter radius for the three different components. The low values of I demonstrate that each component contains sufficient information for identification of the K and n coefficients.

Table 8 shows the identifiability index values obtained when combining the stress components two by two using the following expression for the hessian matrix:

$$\bar{H}_{ij}^{kl,mn} = \sum_{p=0}^N \frac{\partial \bar{\sigma}_{kl}}{\partial \theta_i}(x_p, y_p) \frac{\partial \bar{\sigma}_{kl}}{\partial \theta_j}(x_p, y_p) + \sum_{p=0}^N \frac{\partial \bar{\sigma}_{mn}}{\partial \theta_i}(x_p, y_p) \frac{\partial \bar{\sigma}_{mn}}{\partial \theta_j}(x_p, y_p), \quad (16)$$

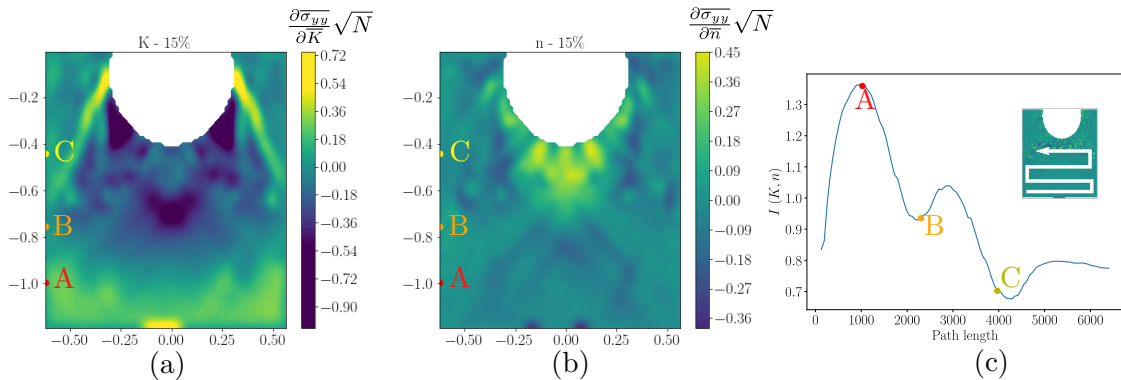


Figure 18: Sensitivity of σ_{yy} to a 15% variation of (a) K and (b) n after applying a low-pass filter with a radius of 10. (c) Evolution of the value of I . Similar conclusions as with σ_{xx} can be drawn.

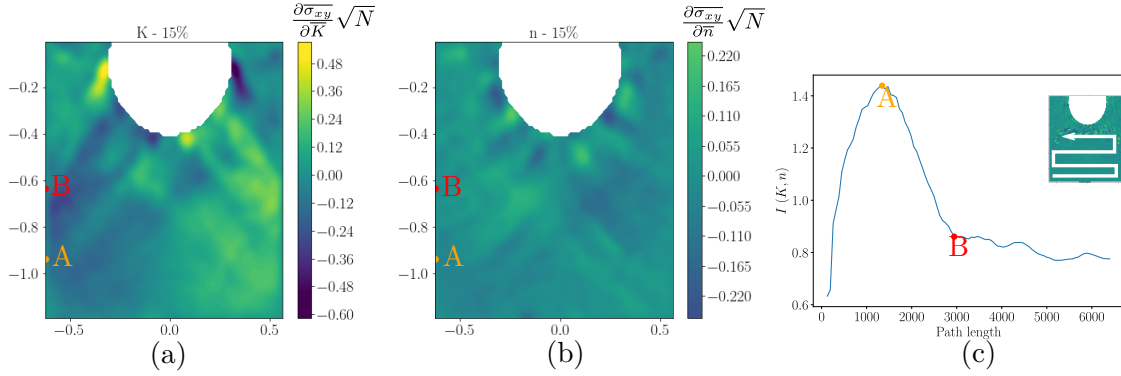


Figure 19: Sensitivity of σ_{xy} to a 15% variation of (a) K and (b) n after applying a low-pass filter with a radius of 10. (c) Evolution of the value of I . The variation of the sensitivity to n up to point A are very subtle. The value of I should therefore be interpreted with great care.

Combining two different components of the residual stress field only slightly enhances the identifiability index value. Finally, combining the three components resulted in $I = 1.3$ which is slightly higher than the best value of I obtained when combining two components of the stress. Thus, adding additional information for identification does not result in a better conditioning of the problem but rather dilutes the relevant information.

Figure 20 (a,c,e) shows the variations of the sensitivity to a 15% variation of K and n on the three components of stress, respectively, on the path presented in Figure 9. For σ_{xx} and σ_{xy} , only small variations of the sensitivity to n are observed along the path, when compared to the sensitivity to K . The sensitivity of the two variables are therefore not as firmly uncorrelated as those observed for σ_{yy} which explains the slightly better value of I found for this stress component. This also explains why combining σ_{xx} and σ_{xy} does not improve the value of I as none of these components provide additional information on the influence of n .

Figure 20 (b,d,f) shows the value of the L_2 norm of the sensitivity for the three components of stress, respectively. All the components are at least three times more sensitive to K than to n , which further explains why different combinations of the stress components did not

Stress component	σ_{xx}	σ_{yy}	σ_{xy}
I	1.4	1.3	1.4

Table 7: Identifiability index values obtained for the different stress components for large Hamming window radius.

Stress component	σ_{yy}	σ_{xy}
σ_{xx}	1.2	1.3
σ_{yy}		1.3

Table 8: Identifiability index values obtained for the different stress components combinations for large Hamming window radius.

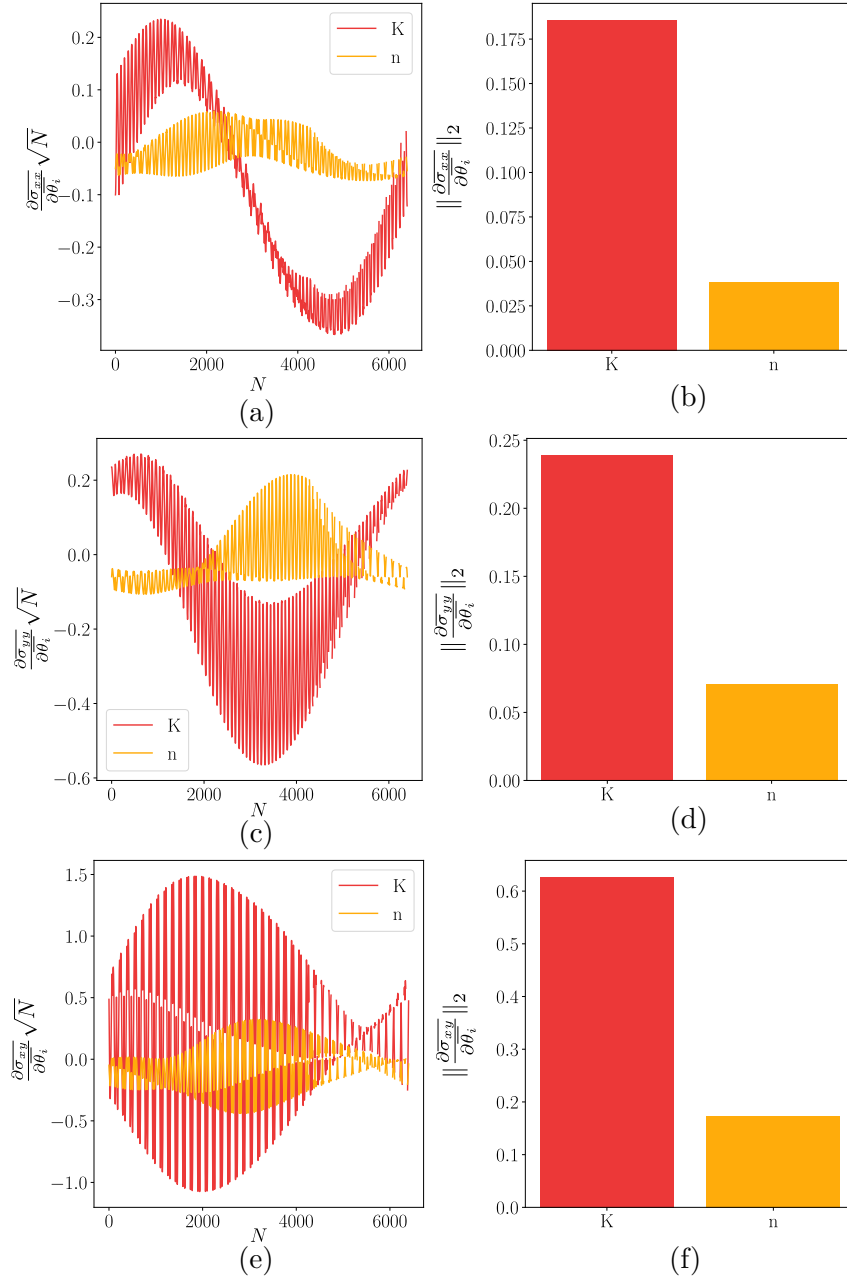


Figure 20: Sensitivity of the (a,b) σ_{xx} , (c,d) σ_{yy} and (e,f) σ_{xy} to a 15% variation of K and n for a shot along the $[100]$ orientation at 40 m s^{-1} . (a,c,e) Evolution of the sensitivity along the path represented in Figure 9. (b,d,f) L_2 norm of the sensitivity. For σ_{xx} and σ_{xy} only small variations of the sensitivity to n are observed along the path when compared to that of the sensitivity to K . All the components are more sensitive to a variation of K than to a variation of n .

result in a better value of I .

Since impact along the $[100]$ orientation and a single impact velocity seems to be sufficient to obtain the values of K and n , identifiability for different velocities and crystal orientations using the residual stress field was not investigated in this work.

3 Discussion

3.1 Identifiability using only the displacement curve

As shown in Figure 6, the effect of K and n can be distinguished respectively by changing the crystal orientation and the shot velocity. This results from the fact that K scales the stress. Its influence thus mainly depends on the stress value, which changes with the orientation. On the other hand, n acts mainly on the strain path. Its influence is therefore more related to the total absorbed energy.

Consequently, when combining two velocities along the same crystal orientation (conditions 1 and 2), only the total energy imposed to the material is varied. Therefore, combining those two tests only provides more information on the effect of n but not on the effect of K . Inversely, combining two different orientations with the same shot velocity only provides more information on the effect of K but not on the effect of n . Consequently, varying the two parameters simultaneously results in the best value of I (2.6) as the influence of both parameters is varied.

Also, combining two displacement curves does not result in an improvement of the value of I in every case. For instance, combining two tests at $40 \text{ m}\cdot\text{s}^{-1}$ along the $[100]$ and $[110]$ orientations results in a similar value of I as when using a single test at $40 \text{ m}\cdot\text{s}^{-1}$. This reveals that no additional information is brought by adding the second test. Renner et al. [22] observed a similar phenomenon when combining two indentation imprint topographies for the identification of two parameters. In some cases, combining the two topographies resulted in a worst value of I than that obtained when using a single topography due to a dilution of the relevant information.

The value of I obtained in this work using only the displacement curve is still too high to assess the problem well-posedness. This might however be sufficient to obtain a first raw estimate of the value of (K, n) that could then be refined using another observation field, such as the residual stresses. This could be confirmed by performing identification on a virtual material using both the displacement curve and the residual stress field.

Also, combining the displacement curve with the residual stress field for the same test results in a lower value of I . The shot displacement is therefore an interesting complementary observation field to use for identification.

Finally, the whole space of crystal orientation and reachable shot velocity should be screened to find the most suitable conditions for identification. This will be performed in future works.

3.2 Identifiability using the residual stress field

Convergence of the sensitivity field in the vicinity of the dent is not achieved in this study, as shown in figure 8. It is interesting to note that the noisy part of the sensitivity field corresponds to the zone where most plastic straining occurred. The more pronounced

stress gradients are therefore also located in this zone. This explains the difficulty to obtain converged sensitivity values under the dent. Experimentally, large plastic strains also prevent stress estimations using HR-EBSD, as they induce noisier diffraction patterns. This zone would therefore also have to be masked on EBSD data and would therefore not be used for identification, even in the absence of numerical convergence issues.

The value of I provided in tables 7 and 8 are those obtained by applying a low-pass filter with a large Hamming window radius on the residual stress field. Applying such filter does not add any information but removes the high frequency noise resulting from numerical uncertainties. However, it also removes parts of the field that should contain relevant information for identification as slight variations of the field could result from a variation of each parameters and not just from the quality of constitutive law integration. Such value of I should therefore be considered as a higher boundary of the identifiability index value.

Each of the three investigated components of the residual stress field contains sufficient information for identification of K and n with a single test in a single orientation with a single shot velocity condition. Combining the different components only results in slight improvements of the identifiability index. This could result from the high Hamming windows radius used for filtering, which could remove parts of the specific relevant information of each field. It could also indicate that the two coefficients have a similar influence on the three components of the stress. Therefore there is no dilution of information when combining two components as each components contains relevant information for identification. However, it does not add any new information on the distinct influence of each parameter and therefore does not really improve the problem conditioning.

Also, using only the bottom of the field, the zone where the most pronounced effects occur is unused. To make better use of the whole residual stress field in future works, identification should not be performed by comparing the target and simulated field point-wise but by comparing well-chosen characteristics of the field. This could for instance be performed by automatically extracting the field characteristic using image segmentation methods [24].

The value of I found for identification of K and n using the residual stress field under the dent ranges from 1.2 to 1.4 depending on the stress component used. Breumier et al. [7] performed similar sensitivity analysis for K and n using high strain rate micropillar compression tests. It revealed that using two stress strain curves at two different strain rate on a single crystal orientation lead to a value of $I = 1.3$. As the residual stress field is a direct consequence of the plastic straining occurring during the impact event, it contains more information than a stress-strain curve which solely represents an average quantification of the material's behaviour. The value of I presented in table 7 are therefore consistent with that of the literature.

The residual stress field under the impact dent therefore contains sufficient information to obtain the viscoplastic parameters with a single simulation. The resulting identification procedure would therefore be more efficient than that using micropillar compression tests as it would require less tests to be modeled. However, HR-EBSD residual stress analyses

remain an experimental challenge. Indeed, it requires a perfect surface preparation with almost no subsurface residual polishing induced hardening, which could be tedious especially on ductile materials such as copper. Also, such analyses remain mainly applicable on large grains or single crystal samples as the elastic residual strain are obtained by comparing the deformed crystal volume with an undeformed reference volume inside the same grain. This study however reveals that the wealth of information provided by such residual stress fields worth the efforts spent in sample preparation.

Also, note that only the residual stress variations in a single two-dimensional cross-section was considered herein. Advances in 3D-EBSD methods [26] could also provide experimental insights in the stress variation in the sample's volume that could enrich the identification problem.

4 Conclusion

The objective of this work was to investigate the possibility to obtain the viscoplastic parameters of the Meric-Cailletaud framework using outputs provided by a shot impact test. The main contributions are as follows:

- Identification of K and n using the shot displacement curve was shown to be an ill-posed problem.
- Combining two impacts along two different crystal orientations with two different shot velocities slightly improved the problem well-posedness as it provided more information on the distinct influence of the two coefficients on the displacement, which resulted in a value of $I = 2.6$.
- A methodology to establish identifiability of the Meric-Cailletaud constitutive parameters using the residual stress field under the impact dent was established.
- Analysis of the stress sensitivity to a variation of K and n and the resulting values of $I = 1.2$ when combining two stress components revealed that the two coefficients could be identified using the residual stress induced by a single impact on a single crystal orientation.
- Combining the residual stress field with its corresponding displacement curve reduced the value of I from $I = 1.4$ when using only the residual stress field to $I = 1.1$. The two observations fields are therefore complementary.

Using the residual stress field induced by an impact could therefore provide a methodology for identification of material parameters at high strain rate as the strain rates involved by such impact could reach the order of 10^5 s^{-1} . Such parameters could then be used for modeling of processes involving such strain rates such as shot-peening.

Also, identification on a virtual material with chosen coefficients will be conducted in future works to assess the convergence of classical optimization algorithm on the solution using different starting points. This will effectively validate the identifiability analysis presented herein.

The possibility to obtain the K and n parameters using only the shot displacement curve is also very promising as it is very easy to obtain experimentally. The whole crystal orientation and reachable shot velocity space will therefore be screened to investigate if particular experimental conditions could be combined to obtain a well-posed problem using the shot displacement.

Finally, the complementarity of the shot displacement and the impact induced residual stress field is a very interesting results as it demonstrates the possibility to combine different outputs of different nature for the same test to enhance the problem well-posedness. It also demonstrates how the identifiability indicator can be used to design relevant experiments for identification and which information is relevant to use and to combine. The complementarity of the residual stress field and shot displacement with the imprint topography and the crystal misorientation field beneath the dent should also be investigated in future works. Indeed, combining these three different outputs could provide sufficient information to obtain more than two plastic constitutive parameters, such as the six interaction matrix coefficients.

Acknowledgment

This work was supported by the Natural Sciences and Engineering Research Council (NSERC) discovery grants Canada Research Chairs programs (grant number, RGPIN-06412-2016). Finally, the authors would like to thank the Region Auvergne-Rhône-Alpes for their financial support within the SCUSI project.

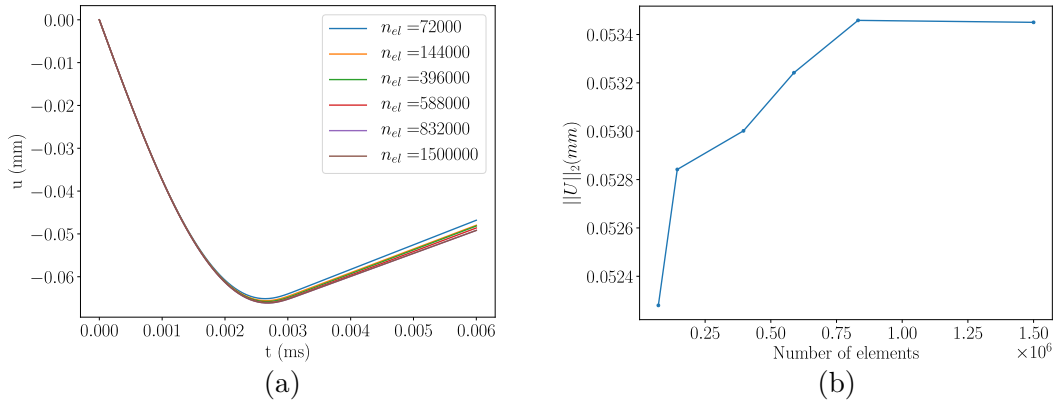


Figure 21: (a) Impact displacement curves obtained for successively refined meshes. (b) Convergence of the L_2 norm of the difference between the displacement curves obtained with two successive meshes. Convergence is observed for simulations with 832 000 elements.

Appendix A: Mesh convergence study

A convergence study was first conducted to reduce the influence of numerical uncertainties on the identification procedure. Figure 21 (a) and (b) respectively shows the displacement curves obtained for successively refined meshes and the evolution of the L_2 norm of the difference between the displacement curves obtained with two consecutive meshes. Convergence can be observed for simulations with 832 000 elements which can be performed in 16h30 using 4 threads on an Intel Xeon Gold 6132, 2.6 GHz CPU with Abaqus 6.14 version.

References

- [1] J. Ast, G. Mohanty, Y. Guo, J. Michler, and X. Maeder. In situ micromechanical testing of tungsten micro-cantilevers using hr-ebcd for the assessment of deformation evolution. *Materials & Design*, 117:265 – 266, 2017.
- [2] A. Barnoush, P. Hosemann, J. Molina-Aldareguia, and J. M. Wheeler. In situ small-scale mechanical testing under extreme environments. *MRS Bulletin*, 44(6):471–477, 2019.
- [3] T. Belytschko, W. K. Liu, B. Moran, and K. Elkhodary. *Nonlinear Finite Elements for Continua and Structures*. Wiley, 2014.
- [4] R. B. Blackman and J. W. Tukey. The measurement of power spectra from the point of view of communications engineering — part i. *Bell System Technical Journal*, 37(1):185–282, 1958.
- [5] S. Breumier. 3deye, <https://doi.org/10.5281/zenodo.4043588>, Sept. 2020.
- [6] S. Breumier. Playing with I , https://colab.research.google.com/github/simonBreumier/Play_with_I/blob/master/Playing%20with%20I.ipynb, 2020.
- [7] S. Breumier, S. Sao-Joao, A. Villani, M. Lévesque, and G. Kermouche. High strain rate micro-compression for crystal plasticity constitutive law parameters identification. *Materials & Design*, 193:108789, 2020.
- [8] S. Breumier, F. Trudeau-Lalonde, T. Lafrance, A. Villani, G. Kermouche, and L. Martin. A shot-peening test rig for controlled single and repeated impact testing in industrial conditions. *submitted in Experimental Mechanics*, 2020.
- [9] S. Breumier, A. Villani, C. Maurice, M. Lévesque, and G. Kermouche. Effect of crystal orientation on indentation-induced residual stress field: simulation and experimental validation. *Materials & Design*, 2018.
- [10] T. Britton, J. Jiang, R. Clough, E. Tarleton, A. Kirkland, and A. Wilkinson. Assessing the precision of strain measurements using electron backscatter diffraction – part 2: Experimental demonstration. *Ultramicroscopy*, 135:136 – 141, 2013.

- [11] O. Casals and S. Forest. Finite element crystal plasticity analysis of spherical indentation in bulk single crystals and coatings. *Computational Materials Science*, 45(3):774 – 782, 2009. Proceedings of the 17th International Workshop on Computational Mechanics of Materials.
- [12] A. Castro Moreno, F. Tu, M. Lévesque, and P. Bocher. Shot peening fem simulation: A novel approach based on crystal plasticity. In *ICSP-13*, 2017.
- [13] K. Ekström. Experimental investigation of the strain rate dependence of ss2506 gear steel. Master’s thesis, KTH, Materials Science and Engineering, 2013.
- [14] A. Giannakopoulos, P.-L. Larsson, and R. Vestergaard. Analysis of vickers indentation. *International Journal of Solids and Structures*, 31(19):2679 – 2708, 1994.
- [15] C. Gérard, G. Cailletaud, and B. Bacroix. Modeling of latent hardening produced by complex loading paths in fcc alloys. *International Journal of Plasticity*, 42(Supplement C):194 – 212, 2013.
- [16] A. Guery, F. Hild, F. Latourte, and S. Roux. Identification of crystal plasticity parameters using dic measurements and weighted femu. *Mechanics of Materials*, 100:55 – 71, 2016.
- [17] W. Johnson. *Impact strength of materials*. Edward Arnold Publishers Limited, 1972.
- [18] U. Kocks and H. Mecking. Physics and phenomenology of strain hardening: the fcc case. *Progress in Materials Science*, 48(3):171 – 273, 2003.
- [19] S. Meguid, G. Sagals, and J. Stranart. 3D finite element analysis of peening of strain-rate sensitive materials using multiple impingement model. *International Journal of Impact Engineering*, 27:119–134, 02 2002.
- [20] L. Méric, G. Cailletaud, and M. Gaspérini. Finite element calculations of copper bicrystal specimens submitted to tension-compression tests. *Acta Metallurgica et Materialia*, 42(3):921 – 935, 1994.
- [21] W. D. Musinski and D. L. McDowell. On the eigenstrain application of shot-peened residual stresses within a crystal plasticity framework: Application to ni-base superalloy specimens. *International Journal of Mechanical Sciences*, 100(Supplement C):195 – 208, 2015.
- [22] E. Renner, A. Bourceret, Y. Gaillard, F. Amiot, P. Delobelle, and F. Richard. Identifiability of single crystal plasticity parameters from residual topographies in berkovich nanoindentation on fcc nickel. *Journal of the Mechanics and Physics of Solids*, 138:103916, 2020.

- [23] F. Richard, M. Villars, and S. Thibaud. Viscoelastic modeling and quantitative experimental characterization of normal and osteoarthritic human articular cartilage using indentation. *Journal of the Mechanical Behavior of Biomedical Materials*, 24:41 – 52, 2013.
- [24] O. Ronneberger, P. Fischer, and T. Brox. U-net: Convolutional networks for biomedical image segmentation. In N. Navab, J. Hornegger, W. M. Wells, and A. F. Frangi, editors, *Medical Image Computing and Computer-Assisted Intervention – MICCAI 2015*, pages 234–241, Cham, 2015. Springer International Publishing.
- [25] T. Rousseau. *Modélisation multi-échelle de la modification de structure d’un alliage à base de nickel soumis à de très fortes déformations plastiques en surface*. PhD thesis, Ecole Centrale de Lyon, 2016.
- [26] N. Zaafarani, D. Raabe, R. Singh, F. Roters, and S. Zaefferer. Three-dimensional investigation of the texture and microstructure below a nanoindent in a cu single crystal using 3d ebsd and crystal plasticity finite element simulations. *Acta Materialia*, 54(7):1863 – 1876, 2006.
- [27] T. Zhang, J. Jiang, S. B.A., T. Britton, and D. F.P.E. Slip localization and fatigue crack nucleation near a non-metallic inclusion in polycrystalline nickel-based superalloy. *Materials Science and Engineering: A*, 641:328–339, 2015.